

Article

Uptake of BF Dye from the Aqueous Phase by CaO-g-C₃N₄ Nanosorbent: Construction, Descriptions, and Recyclability

Ridha Ben Said ^{1,2,*}, Seyfeddine Rahali ¹, Mohamed Ali Ben Aissa ¹, Abuzar Albadri ³ and Abueliz Modwi ¹¹ Department of Chemistry, College of Science and Arts, Qassim University, Ar Rass, Saudi Arabia² Laboratoire de Caractérisations, Applications et Modélisations des Matériaux, Faculté des Sciences de Tunis, Université Tunis El Manar, Tunis 2092, Tunisia³ Department of Chemistry, College of Science, Qassim University, Buraydah 52571, Saudi Arabia

* Correspondence: 141255@qu.edu.sa

Abstract: Removing organic dyes from contaminated wastewater resulting from industrial effluents with a cost-effective approach addresses a major global challenge. The adsorption technique onto carbon-based materials and metal oxide is one of the most effective dye removal procedures. The current work aimed to evaluate the application of calcium oxide-doped carbon nitride nanostructures (CaO-g-C₃N₄) to eliminate basic fuchsin dyes (BF) from wastewater. CaO-g-C₃N₄ nanosorbent were obtained via ultrasonication and characterized by scanning electron microscopy, X-ray diffraction, TEM, and BET. The TEM analysis reveals 2D nanosheet-like nanoparticle architectures with a high specific surface area (37.31 m²/g) for the as-fabricated CaO-g-C₃N₄ nanosorbent. The adsorption results demonstrated that the variation of the dye concentration impacted the elimination of BF by CaO-g-C₃N₄ while no effect of pH on the removal of BF was observed. Freundlich isotherm and Pseudo-First-order adsorption kinetics models best fitted BF adsorption onto CaO-g-C₃N₄. The highest adsorption capacity of CaO-g-C₃N₄ for BF was determined to be 813 mg·g⁻¹. The adsorption mechanism of BF is related to the π-π stacking bridging and hydrogen bond, as demonstrated by the FTIR study. CaO-g-C₃N₄ nanostructures may be easily recovered from solution and were effectively employed for BF elimination in at least four continuous cycles. The fabricated CaO-g-C₃N₄ adsorbent display excellent BF adsorption capacity and can be used as a potential sorbent in wastewater purification.

Keywords: calcium oxide-doped carbon nitride nanostructures; basic fuchsin; elimination mechanism; π-π stacking



Citation: Said, R.B.; Rahali, S.; Ben Aissa, M.A.; Albadri, A.; Modwi, A. Uptake of BF Dye from the Aqueous Phase by CaO-g-C₃N₄ Nanosorbent: Construction, Descriptions, and Recyclability. *Inorganics* **2023**, *11*, 44. <https://doi.org/10.3390/inorganics11010044>

Academic Editor: Roberto Nisticò

Received: 5 November 2022

Revised: 9 January 2023

Accepted: 11 January 2023

Published: 16 January 2023



Copyright: © 2023 by the authors. Licensee MDPI, Basel, Switzerland. This article is an open access article distributed under the terms and conditions of the Creative Commons Attribution (CC BY) license (<https://creativecommons.org/licenses/by/4.0/>).

1. Introduction

Water pollution is one of the most important environmental hazards in the modern world, caused by wastewater discharge, insufficient treatment methods, and leakage into the natural water cycle [1,2]. Depending on the source, such as industrial plants, wastewater streams can contain excessively polluting components. Organics [3] (phenolic compounds, dyes, halogenated compounds, oils, etc.) and heavy metals (Hg, Cd, Pb, Cr, Ag, etc.) [4] are potential contaminants in wastewater, as they are biodegradable, volatile, and recycled organic compounds, suspended particles, pathogens, and parasites. Most chemical dyes are probable carcinogens [5]. Thus, before discharging wastewater, it is important to lessen or remove the presence of these potentially fatal substances.

Among these dyes, basic fuchsin BF is a triarylmethane dye that is inflammable and has antibacterial and fungicidal characteristics [6,7]. It is commonly employed as a colorant in textile and leather goods as well as in the staining of collagen and tubercle bacillus [8]. Because of its low biodegradability and its toxicity, carcinogenicity, and unsightliness [9–11], Basic Fuchsin removal from wastewater systems is a major concern that should be studied and executed as soon as possible.

In addition to the traditional biological, electrochemical, and photocatalytic oxidation and decomposition routes, physical processes (such as adsorption) are common methods that have also been developed and are used to remove organic pollutants from wastewater streams [12–14]. Even though these technologies can turn organic pollutants into non-hazardous molecules and can be used in various ways, their inability to be scaled up is a significant problem from an engineering point of view.

More specifically, the adsorption method was widely regarded as the most effective way to treat dye wastewater because of its significant adsorption capacity, low cost, good selectivity, and ease of operation [15–18]. Therefore, many researchers invest a lot of time and effort into creating new adsorbents, as well as adsorption mechanisms and treatment technology, in the hopes that they would be more useful in the treatment of dye wastewater [19–21].

Besides, graphitic carbon nitride ($g\text{-C}_3\text{N}_4$) nanosheet has been identified as an indispensable material for two-dimensional structures due to its graphitic-like structure and high stability under ambient circumstances [22]. It is composed of carbon and nitrogen and is most commonly employed for energy conversion and storage. Its π conjugated polymeric metal-free semiconducting 2D structure is composed of graphitic planes composed of sp^2 -hybridized carbon and nitrogen [23]. Because $g\text{-C}_3\text{N}_4$ contains a sufficient number of edge amino and amino groups (NH/NH_2), it can supply several binding sites. Therefore, $g\text{-C}_3\text{N}_4$ is regarded as a suitable adsorbent for removing pollutants from wastewater. Nevertheless, $g\text{-C}_3\text{N}_4$ nanosheets capability to adsorb is limited by its small surface area and few functional groups [24].

Therefore, the development of $g\text{-C}_3\text{N}_4$ -containing compounds with higher photonic efficiency, such as TiO_2 and ZnO , piqued the curiosity of a vast number of researchers [25,26]. This was accomplished by combining $g\text{-C}_3\text{N}_4$ with another semiconductor and decorating $g\text{-C}_3\text{N}_4$ with noble metals [27–31]. Construction of heterojunctions comprised of $g\text{-C}_3\text{N}_4$ mixed with another type of compound, such as CaO nanomaterials, and preparation of a Ca-O doped with $g\text{-C}_3\text{N}_4$ with an improved surface texture by selecting the optimal preparation method are the most beneficial means of enhancing the adsorption properties of $g\text{-C}_3\text{N}_4$.

In the current study, a mesoporous $\text{CaO}@g\text{-C}_3\text{N}_4$ nanocomposite was successfully produced using a simple sonochemical process and evaluated as a promising adsorbent material for adsorbing the basic fuchsin dye from a contaminated aqueous phase. The physicochemical relationship between characterizations and measurements of equilibrium and kinetics was studied. Adsorption isotherm data were also modeled, and the adsorption performance of $\text{CaO}@g\text{-C}_3\text{N}_4$ nanocomposite for basic fuchsin was investigated.

2. Experimental

2.1. Chemicals

Sodium hydroxide (NaOH , $\geq 99\%$), sodium chloride (NaCl , $\geq 99\%$), basic fuchsin (BF, $\geq 85\%$), urea ($\text{CH}_4\text{N}_2\text{O}$, $\geq 98\%$) and calcium carbonate (CaCO_3 , $\geq 99\%$) purchased from Merck Company were used without further purification. The required dyes concentrations (25, 50, 100, 150, 200, and 300 ppm) were obtained by diluting BF stock solution (500 ppm).

2.2. $\text{CaO-g-C}_3\text{N}_4$ Nanosorbent Fabrication

The nanosheets of $g\text{-C}_3\text{N}_4$ were produced through the thermal breakdown of urea. In a typical technique, 0.075 moles of a carbamide compound were placed in a covered pot and tempered with a heating rate of $10\text{ }^\circ\text{C}/\text{min}$ at 723 K for 120 min. The produced yellow raw $g\text{-C}_3\text{N}_4$ was then cooled, pulverized, and stored in a dark container. Thermally decomposing carbonate salts created calcium oxide (CaO) nanoparticles. Two grams of calcium carbonate salts were weighed, placed in a crucible, and annealed at 1073 K for one hour. $\text{CaO-g-C}_3\text{N}_4$ nanoparticles were produced using a step-by-step ultrasonication technique aided by an organic solvent (ethanol). In 125 mL of ethanol, 2.76 mg of $g\text{-C}_3\text{N}_4$ was sonicated for 15 min. CaO nanoparticles were added to the $g\text{-C}_3\text{N}_4$ ethanolic solution

along with an additional 45 min of sonication. The yellowish solution generated was evaporated at 368 K for 1440 min. CaO-g-C₃N₄ nanosorbent was ultimately tempered at 453 K for 60 min.

2.3. CaO-g-C₃N₄ Nanosorbent Characterizations

The nanosorbent CaO-g-C₃N₄ was studied using a variety of analytical and spectroscopic techniques. Energy dispersive X-ray (EDX) spectroscopy was used to calculate the elemental composition of the CaO-g-C₃N₄ nanosorbent. The transmission electron microscope (Tecnai G20-USA) was used to make morphological observations, and the stimulating voltage was set at 200 kV. X-ray diffraction (XRD) was used to analyze the phase structure using a Bruker D8 Advance diffractometer Cu-K ($\lambda = 1.540$) radiation source. An ASAP 2020 device was used to evaluate the accurate analysis of the surface area. Before and after the BF dye elimination, Fourier transformed infrared (FTIR) spectra were recorded using a Nicolet 5700 spectrometer equipped with a KBr pellet.

2.4. BF Dye Removal Experiments

By mixing 25 mL of BF dye solution with 10 mg of CaO-g-C₃N₄ nanosorbent at varying starting concentrations (5–300 mg/L), batch removal tests of BF dye were conducted. In order to attain equilibrium, the set mixture was stirred for 24 h at 400 rpm. After centrifugation, a clear solution was produced. The dye volumes and beginning concentrations were 100 mL and 250 ppm, respectively, for the kinetic experiment, and the CaO-g-C₃N₄ nanosorbent mass was 40 mg. The test was conducted in the dark with magnetic stirring. Later, 10 mL of the suspension was withdrawn and centrifuged for 10 min to measure the remaining concentration of BF dye.

Using a spectrophotometer, the concentration of dye was determined, and equilibrium dye capacity (q_e) was calculated using the following equation:

$$q_e = \frac{C_0 - C_e}{m} \cdot v \quad (1)$$

where q_t (mg·g⁻¹) is the quantity of dye removed by a unit mass of nanosorbent m (g) at a specified interval of time (min), V is the volume of the solution (L), C_0 is the initial dye concentration, and C_t is the concentration at time t (mg L⁻¹). A similar calculation was used to compute the amount adsorbed at equilibrium, q_t :

$$q_t = \frac{C_0 - C_t}{m} \cdot v \quad (2)$$

The influence of the dye's elimination on the pH of the aqueous media was investigated by setting the initial pH value of dye solution from 3 to 11 pH range by using either NaOH (0.1 mole·L⁻¹) or HCl (0.1 mole·L⁻¹). The pH of zero-point charge (pHzpc) for CaO-g-C₃N₄ nanosorbent was evaluated by the salt addition approach. A fixed amount of CaO-g-C₃N₄ nanosorbent (20 mg) was added in each flask containing 20 mL NaCl solution (0.01 M) with pH initial (pHi) values raised from 2 to 12 (by adjustments using 0.1 M NaOH or HCl solutions). The mixture was stirred for one hour, and the final pH (pH_f) was calculated after eliminating CaO-g-C₃N₄ by filtration. For the reusability test, the CaO-g-C₃N₄ nanosorbent used after the adsorption experiments was recovered by filtration and then calcined at 773 K. for one hour. After that, the recovered CaO-g-C₃N₄ nanosorbent was reused for further adsorption tests.

3. Results and Discussion

3.1. CaO-g-C₃N₄ Nanosorbent Characterizations

The scanning elemental mapping analysis for Ca, N, O, and C in the CaO-g-C₃N₄ nanosorbent aggregates (Figure 1a–e) indicates an overall homogeneous dispersion, as shown in Figure 1b–e. On the elemental maps, a brighter zone implies a higher elemental ratio. The CaO-g-C₃N₄ nanocomposite has created a homogenous distribution, according

to this observation. An image taken using EDX identifies the individual components that are present in CaO-g-C₃N₄ nanosorbent material. As a result, it is clear from the findings of the EDX performed on CaO-g-C₃N₄ nanosorbent that the surface is composed of carbon (C), nitrogen (N), calcium (Ca), and oxygen (O). These findings are because the results depict bands corresponding to each component (Figure 1a–f).

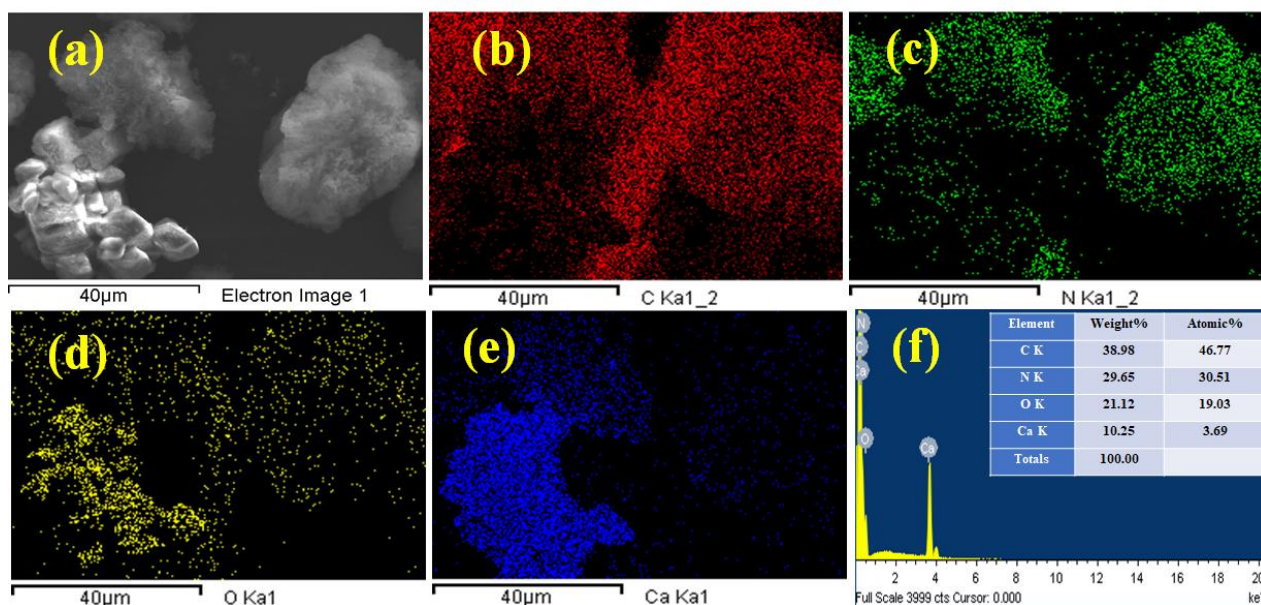


Figure 1. (a–e) Elemental mapping distribution and (f) EDX graph of CaO-g-C₃N₄ nanosorbent.

The TEM micrograph was utilized to investigate the textural qualities of the fabricated CaO-g-C₃N₄ nanosorbent. The TEM photographs of the CaO, g-C₃N₄, and CaO-g-C₃N₄ nanostructures are depicted in Figure 2. The TEM image of CaO (Figure 2a) presents like-sheets shape nanoparticles. On the other hand, the TEM image of g-C₃N₄ (Figure 2b) displays layers with soft surface sheets as a typical graphitic nanostructure [32]. Furthermore, the images with different magnifications obtained from the TEM of the CaO-g-C₃N₄ demonstrated that the morphology had an apparently random appearance, as given in (Figure 2a–d). The CaO-g-C₃N₄ nanosorbent exhibits characteristic 2D nanosheet-like nanoparticle architectures, as seen in (Figure 2a–d). The average particle size of the CaO nanoparticles integrated into the CaO-g-C₃N₄ nanosorbent is around 20–60 nm. CaO are observed to be well disseminated on the g-C₃N₄ surface, forming an abundance of self-active sites on the nanosorbent surface.

Figure 3 depicts the typical peaks at 12.92° and 27.64° for g-C₃N₄ in the XRD pattern. The first peak corresponds to the in-plane packing of tris-triazine units with a d-spacing of 0.685 nm, which agrees with the distance between holes in the nitride pores. However, the great peak at 27.64° is associated with C–N aromatic stacking units separated by 0.322 nm, which corresponds to the 002 interlayer layering plane of the connected aromatic system [33]. Alternatively, the peaks 32.14, 37.25, 53.77, 64.00, and 67.30° correspond to the (110), (200), (202), (311), and (222) planes of the cubic phase of CaO (XRD file JCPDS 77-2376) [34]. Besides the CaO peaks, Ca(OH)₂ and CaCO₃ peaks are seen at 18.00°, 29.32°, 47.39°, and 48.40°, respectively. The presence of calcite (CaCO₃) and hydroxide peaks indicates incomplete pyrolysis of the precursor and fast carbonation and hydrolysis of CaO by ambient CO₂ and water vapor. Literature indicates that CaO nanoparticles have a strong potential for capturing greenhouse gas CO₂ [35]. Finally, the XRD pattern obtained from the fabricated indicates the presence of the g-C₃N₄ and CaO peaks (Figure 3), implying the construction of the target nanosorbent.

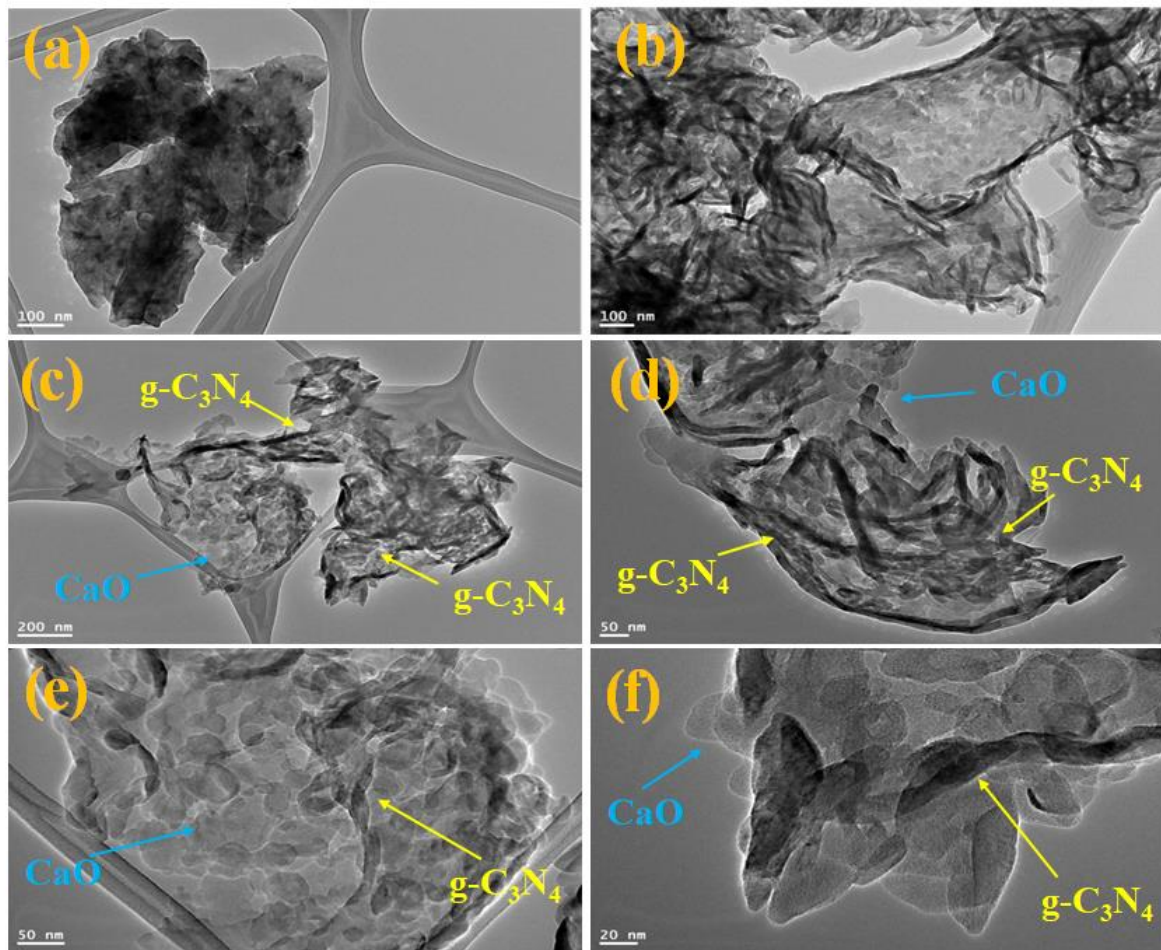


Figure 2. TEM images of (a) CaO, (b) g-C₃N₄, and (c–f) CaO-g-C₃N₄ nanosorbent with different magnifications.

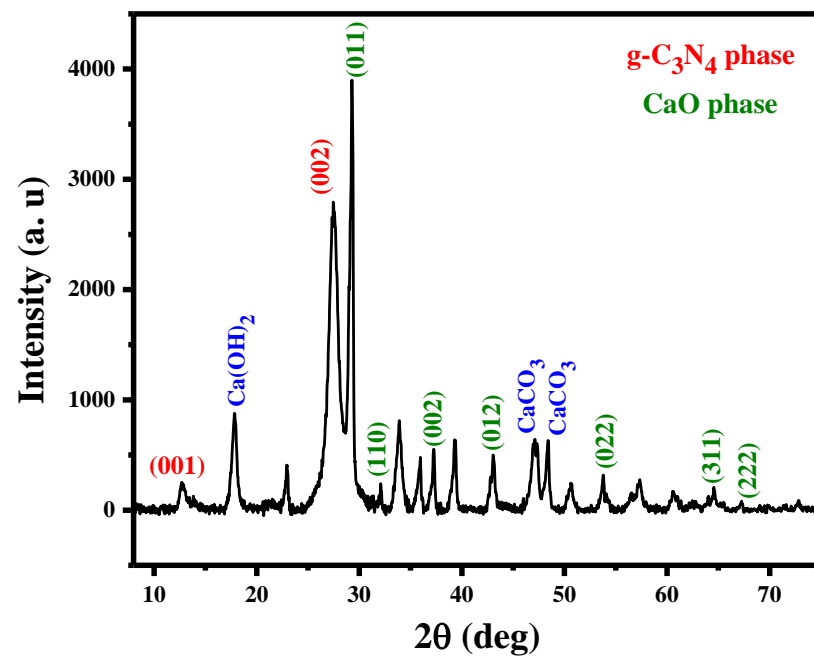


Figure 3. XRD patterns of CaO-g-C₃N₄ nanosorbent.

Nanomaterials utilized as adsorbents are profoundly influenced by their particular surface area and porous structure, which can provide additional adsorption and reactive sites. The N₂ absorption-desorption isotherms of CaO-g-C₃N₄ nanosorbent, which may be categorized as type IV according to the IUPAC system, were determined [36]. Figure 4a,b displays the BET surface isotherms and pore size distribution of the CaO-g-C₃N₄ nanosorbent as manufactured. According to the results, the CaO-g-C₃N₄ nanosorbent absorption-desorption graphs fit isotherm type IV and the hysteresis loop (H₂) for relative pressures between 0.0 and 1.0. This result confirmed the mesoporous nature of the CaO-g-C₃N₄ nanosorbent [37,38]. Due to the presence of several active sites on the surface, the CaO-g-C₃N₄ nanosorbent increased surface area, demonstrated by a higher specific surface area (37.31 m²/g) with a pore volume of 0.136 cc/g, will improve the sorption capacity [39].

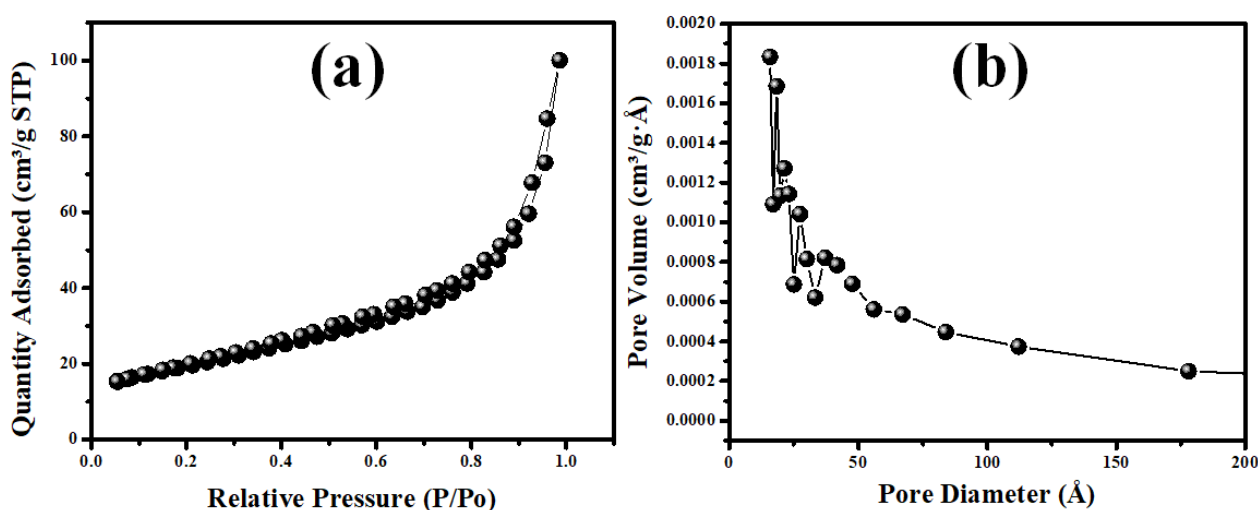


Figure 4. (a) BET surface isotherms and (b) pore sizes distribution of the CaO-g-C₃N₄ nanosorbent.

The chemical condition of the elements on the surface of the CaO@g-C₃N₄ nanostructure was determined by XPS analysis; see Figure 5a–d. CaO exists because the Ca 2p peaks at 349 and 352.6 eV correspond to the divalent oxidation states of calcium oxygen molecules (Ca-2p_{3/2} and Ca-2p_{1/2}) [40,41]. Ca-O and hydroxyl groups in water molecules correspond to the three O 1s peaks detected at 532.6, 533.7, and 534.4 eV which correspond to the lattice oxygen of the layer-structured Ca-O, and adsorbed H₂O or surface hydroxyl oxygen, respectively (Figure 5b) [42]. As shown in Figure 4c, carbon in the C-C and N-C=N states is attributed with two distinct contributions at 285.8 and 288.2 eV, respectively. According to the XPS analysis, only Ca, O, C, and N are present. The peaks at 398.8 and 400.3 eV (Figure 5d) for N 1s which indicate, respectively, the sp² hybridized carbon–nitrogen bonding in (C–N) and N–O of the CN and the binding energy of the N atoms in C–N–C [43]. The absence of other impurity peaks supports the results of the XRD and EDS studies.

3.2. BF Removal onto CaO-g-C₃N₄ Nanosorbent

3.2.1. Impact of Variation pH on BF Removal by CaO-g-C₃N₄ Nanosorbent

The solution's pH controls the adsorbent's sorption affinity by adjusting the surface charge and the ionizing strength of the adsorbent [44]. Adsorption experiments of CaO-g-C₃N₄ nanosorbent were conducted under various initial pH values in order to demonstrate the impact of pH value on the adsorption of BF dyes (from 3 to 11). Figure 6a illustrates the influence of pH on BF uptake. It was discovered that BF dyes may be stably adsorbed without observable alterations. The zero-point charge experiment was performed to explain the acquired results. The pH_{zpc} of CaO-g-C₃N₄ nanosorbent is determined to be 10.6, as shown in Figure 6b. At lower pH, the surface of the CaO-g-C₃N₄ nanosorbent is positively charged and becomes negative at pH greater than pH_{zpc} (=10.6). The pH studies showed that the adsorption is pH-independent, indicating that the electrostatic interactions do not

control the adsorption mechanism. The adsorption was likely due to the formation of H bonding between -OH and -NH₂ onto the CaO-g-C₃N₄ surface with BF dye molecules [45].

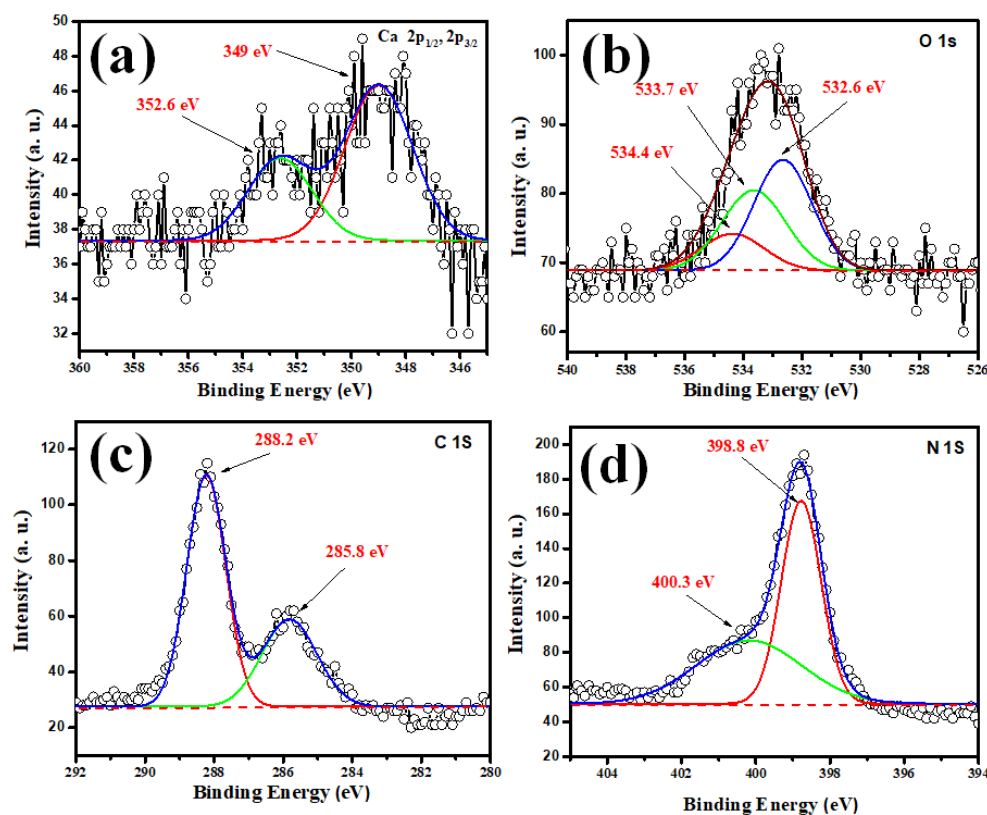


Figure 5. XPS spectra of (a) Ca-2p; (b) O 1s; (c) C 1s and (d) N 1s for CaO@g-C₃N₄ nanosorbent.

3.2.2. Influence of the Initial BF Dye Concentration and Doping

The influence of the initial BF dye concentration in the range of 5–300 mg/L on the adsorption efficiency of CaO-g-C₃N₄ nanosorbent was scrutinized under the following operating conditions: contact time 1440 min, room temperature, pH 7, 400 rpm stirring speed, and a CaO-g-C₃N₄ sorbent dose of 10 mg. As shown in Figure 6c, increasing the initial BF concentration from 5 to 300 mg/L improved the adsorption capacity significantly from 60.61 to 738.08 mg/g. These results indicate that BF molecules in the reaction medium interact more strongly with the top layer of the CaO-C₃N₄ sorbent particles at lower concentrations due to a large amount of vacant active sites. Conversely, the ratio of accessible sites for BF molecules declines with a further rise in the concentration attributed to saturation. To compare the BF dye adsorption capacities of g-C₃N₄ and CaO-g-C₃N₄, a series of adsorption experiments were conducted at different initial BF concentrations and a pH value of 7. The obtained results are also shown in Figure 6c. It is interesting to remark that CaO-g-C₃N₄ exhibits higher BF adsorption capacity than the respective capacities of pure g-C₃N₄ for the different initial BF concentrations. This result demonstrates that g-C₃N₄ nanosheets have the capability to adsorb is limited by its small surface area and few functional groups. The doping of g-C₃N₄ by CaO enhances the adsorption properties of g-C₃N₄ by improving surface texture.

3.2.3. Adsorption Equilibrium of BF Dyes onto CaO-C₃N₄ Nanosorbent

The greatest amount of BF absorbed by CaO-g-C₃N₄ nanosorbent is a crucial characteristic for assessing the high adsorption capacity exhibited. To estimate the adsorption capacity of CaO-g-C₃N₄ nanosorbent, two adsorption isotherm models (Freundlich and Langmuir) were utilized to assess the adsorption data, as depicted in Figure 7a,b. Table 1 contains the formulas corresponding to each isotherm model and the derived parameters.

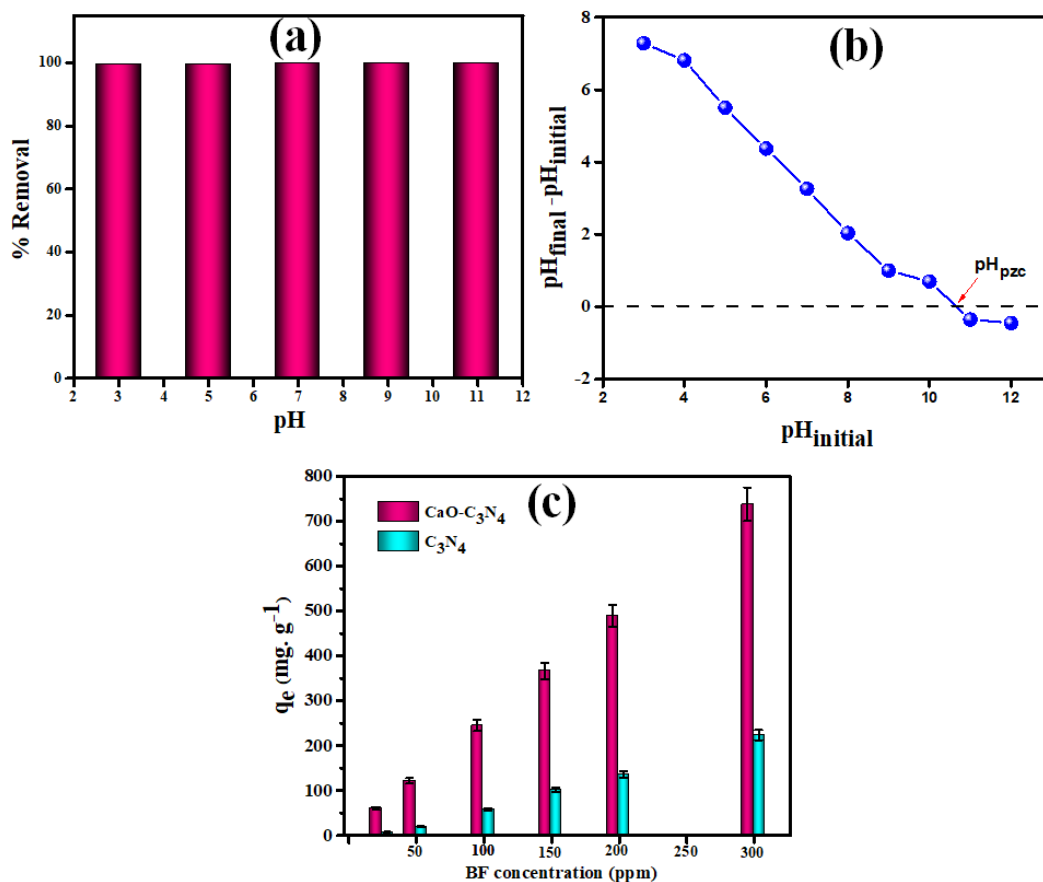


Figure 6. (a) Effect of pH on % removal of BF, (b) plot for the determination of pH_{pzc} for CaO-g- C_3N_4 nanosorbent, and (c) influence of dye concentration onto the adsorption capacity of CaO-g- C_3N_4 and g- C_3N_4 nanosorbent.

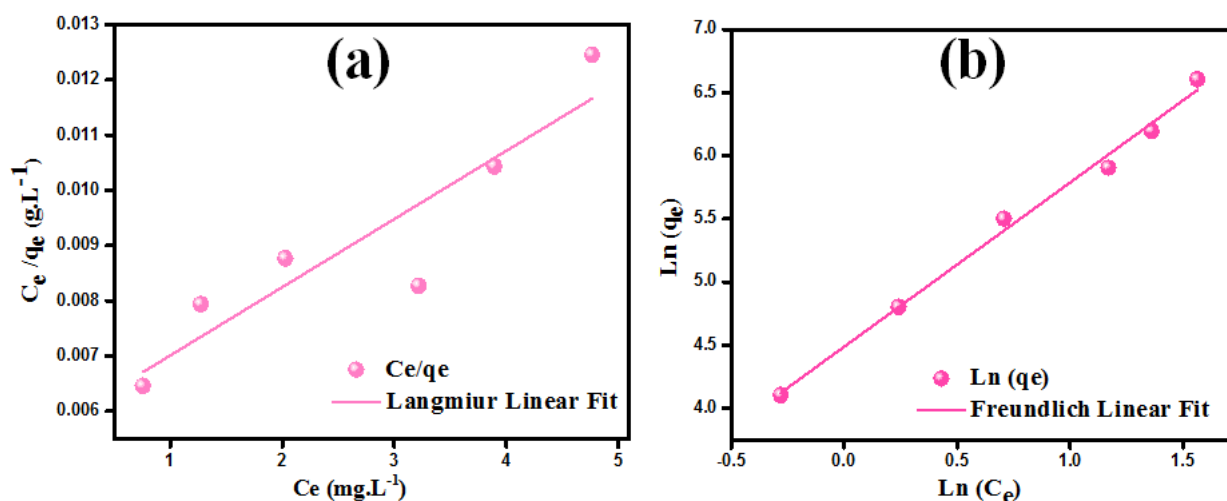


Figure 7. Experimental and fitted adsorption data using the Freundlich (a) and Langmuir (b) models.

As can be noted from the isotherm graphs and the experimental data for BF adsorption over CaO- C_3N_4 nanosorbent, the Freundlich adsorption isotherm has the highest $R^2 = 0.996$. These findings indicate that the Freundlich adsorption isotherm curve is more accurate to fit the experimental data.

Table 1. Used equilibrium isotherm models for the adsorption of BF onto CaO-g-C₃N₄ nanosorbent.

Equilibrium Models	Linear Form	Parameter	Value
Langmuir [46]	$\frac{C_e}{q_e} = \frac{1}{q_m K_L} + \frac{C_e}{q_m}$	q_m (mg/g)	813.0
		K_L (mg/g)	0.212
		R_L (L/mg)	0.0015
		R^2	0.842
		Freundlich [47]	$\ln q_e = \ln K_F + \frac{1}{n} \ln C_e$
		K_F (L/mg)	88.89
		R^2	0.996

The greatest sorption capacity of CaO-g-C₃N₄ nanosorbent for BF dyes is found to be 813 mg·g⁻¹, as given in Table 1.

3.2.4. BF Contact Time and Adsorption Kinetic Studies

Figure 8a shows the relationship between contact time and BF adsorption on the surface of the CaO-C₃N₄ nanosorbent. Adsorption capacity is seen to increase with longer contact times, reaching equilibrium after 25.9 min. Beyond this equilibrium threshold, the adsorption capacity and the amount of BF adsorbed are in dynamic equilibrium. BF molecules were rapidly adsorbed by CaO-C₃N₄ nanosorbent for the first 25.9 min, after which the adsorption rate declined until it reached its maximum value at around 1440 min. The initial adsorption rates are relatively high due to the abundance of active sites on the surface of the CaO-g-C₃N₄. After attaining equilibrium, the active site concentration falls, and dye adsorption does not occur.

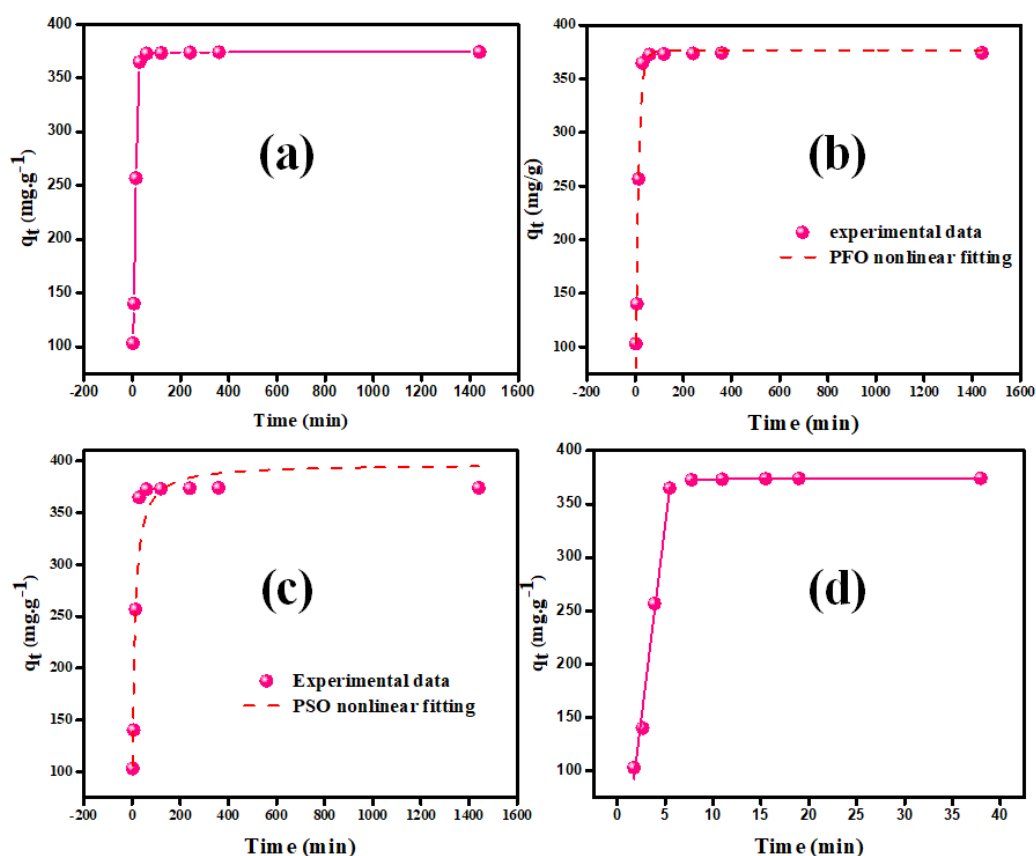


Figure 8. (a) Equilibrium time study (b) PFO, (c) PSO and (d) Intra-particle diffusion graphs for the uptake of BF onto CaO-g-C₃N₄.

The adsorption kinetics measures the rate of solute adsorption at the solid–liquid interface and gives essential information on the equilibrium period for the design and management of an adsorption process [48]. As shown in Figure 8b,c, the BF adsorption kinetics by the CaO-g-C₃N₄ nanosorbent was investigated using pseudo-first-order (PFO) and pseudo-second-order (PSO) kinetic models (b and c). The form of the relevant nonlinear equations is shown in Table 2.

Table 2. Kinetics models for BF adsorption onto CaO-g-C₃N₄ nanosorbent.

Kinetics Models	Kinetic Equations	Parameter	Value
PFO [49]	$q_t = q_e (1 - e^{-k_1 t})$	Q_m (exp) (mg/g)	375.69
		Q_e (mg/g)	376.49
		K_1 (min ⁻¹)	0.080
		R^2	0.984
PSO [49]	$q_t = \frac{t k_2 q_e^2}{k_2 q_e t + 1}$	Q_e (cal) (mg/g)	397.13
		K_2 (g/mg·min)	0.0003
		R^2	0.930
		K_{dif1} (mg·min ^{1/2} /g)	72.78
Intra-particle Diffusion [50]	$q_t = k_{dif} \sqrt{t} + C$	C_1	33.53
		R^2	0.987
		K_{dif2} (mg·min ^{1/2} /g)	0.04
		C_2	372.83
		R^2	0.643

The computed model parameters under the experimental conditions tested are summarized in Table 2. The PFO model might adequately describe the experimental adsorption kinetics data. It claims that the ratio of the square of the number of accessible sites to the rate of adsorption site occupancy. The form formula for the PFO nonlinear linear model is shown in Table 2. Using the computed model parameters in Table 2, the extraordinarily high R^2 value of 0.984 is determined. Compared to the PSO, the PFO equation provides a perfect fit, as shown by the findings. For the tested BF concentrations, there is only a small difference between the experimental Q_{max} values and the model-estimated Q_{max} values. As a result, the PFO model's best fit implies that the kinetic adsorption may be mathematically described using the concentration of BF in solution [44,51].

Through the intra-particle diffusion/transport mechanism, the BF elimination may be transferred from the bulk of the solution to the solid phase of the CaO-g-C₃N₄ nanosorbent. In some circumstances, the step of the adsorption process known as intra-particle diffusion is restrictive. The diffusion pattern developed by Weber and Morris supports the notion of intra-particle diffusion [52,53]. As q_t and $t^{1/2}$ are compared linearly, the removal of BF onto the CaO-C₃N₄ surface demonstrates the efficacy of the intra-particle diffusion kinetic pattern. In addition, the intra-particle mode of diffusion is characterized by the regression coefficient ($R^2 = 0.987$). The diameter of the boundary layer is represented by parameter C 's value. The higher percentages of the constants in Table 2 demonstrate the solution boundary layer's strong influence on the removal of BF dyes [52,53]. It can be seen that the first stage of sorption has a larger rate than the second phase, which is shown by $k_{dif1} > k_{dif2}$ (Table 2). The high value of the rate produced by the first step may be explained by the movement of the dye mover through the solution and onto the surface of the outer CaO-g-C₃N₄ that is generated by the boundary layer. Comparatively, the subsequent phase describes the last equilibrium step, when intra-particle diffusion begins to diminish due to the solute's modest concentration gradient and the restricted number of holes and pores available for diffusion [54].

3.3. Regeneration and Reusability Study

By removing BF from the surface of the nanomaterial, the reusability and regeneration of CaO-g-C₃N₄ sorbent were investigated. Following the adsorption experiment, the BF

was removed from the CaO-g-C₃N₄ by heating it in an oven at 773 K for a one hour. The recovered CaO-g-C₃N₄ was then reapplied to the BF elimination process. CaO-g-C₃N₄ has been used efficiently for the removal of BF for at least four continuous cycles, as shown by the reusability results (Figure 9a). As shown, there was no obvious decrease in the elimination effectiveness during four adsorption–desorption cycles, and only 4%, 7%, and 9% of the adsorption capacity for BF declined at the second, third, and fourth cycles, respectively.

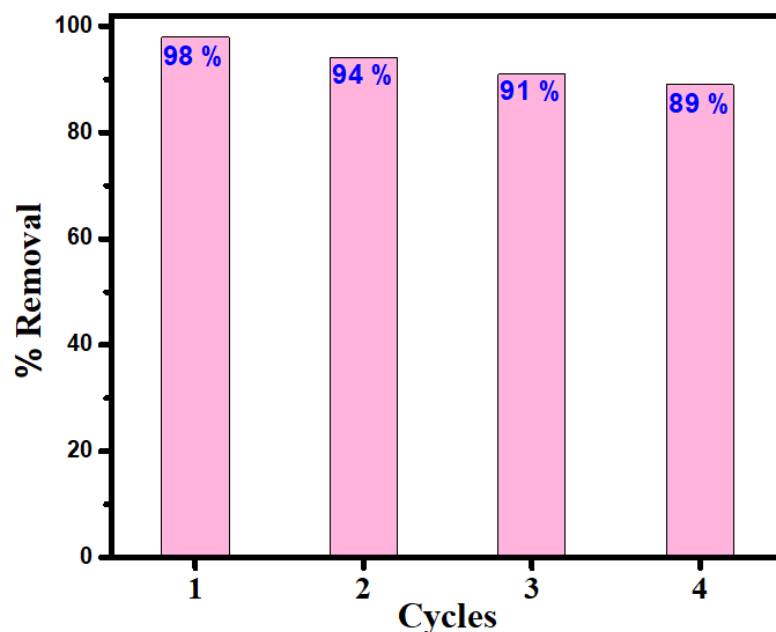


Figure 9. Reusability effectiveness of CaO-g-C₃N₄.

3.4. Comparison Study

As shown in Table 3, the calculated adsorption capacity of CaO-g-C₃N₄ for BF using the Langmuir isotherm model is 813.00 mg·g⁻¹. It is to one's advantage to evaluate the CaO-g-C₃N₄ adsorption capacity in relation to the diverse sorbents that can be utilized for BF elimination. Table 3 shows the various sorbents with high adsorption capacities for BF removal. Compared to previously reported sorbents like MgO and modified activated carbons, CaO-g-C₃N₄ has a higher capacity for adsorption. This finding confirmed that CaO-g-C₃N₄ is an efficient BF dye adsorbent.

Table 3. Observation of adsorption capacities of the CaO-g-C₃N₄ using various nanomaterial adsorbents.

Adsorbents	q _e (mg g ⁻¹)	Best pH	BET Surface Area (m ² /g)	References
Fe-MgO/kaolinite	10.36	9.0	-	[55]
YZnO nanoparticles	75.53	11	20.26	[56]
Al/MCM-41	54.44	3–9	997	[57]
Euryale ferox Salisbury seed shell	19.48	6.0	-	[58]
ESM	47.85	6.0	11.56	[59]
Fe/ZSM-5	251.87	5.0	399	[60]
Modified activated carbons	238.10	8.5	613	[61]
MgO	493.90	11	12.22	[62]
MgO-g-C ₃ N ₄	1250	7.0	84.2	[63]
CaO-g-C ₃ N ₄	813.00	Independent	37.31	Current study

3.5. Adsorption Mechanism

The adsorption mechanism of BF dyes by nanosorbent has been elucidated using FTIR analysis. Figure 10a depicts the FTIR spectra of nanosorbent prior to and following BF adsorption. CaO-g-C₃N₄ spectrum reveals a number of distinguishable bands: the

bandwidth between 3000 and 3600 cm^{-1} corresponds to the stretching vibration modes of O–H and NH. The absorption bands at 1242, 1326, and 1412 cm^{-1} are associated with aromatic C–N stretching, while the absorption bands at 1578 and 1640 cm^{-1} are associated with C \equiv N stretching. The band at 884 cm^{-1} corresponds to the triazine ring mode, a frequent carbon nitride mode. The characteristic band located at 805 cm^{-1} is assigned to Ca–O vibration mode [64]. After adsorption, as can be observed in Figure 10a, many typical BF bands form and move around with respect to the free molecules, suggesting that CaO-g-C₃N₄ and BF molecules may interact. Also, following the adsorption of BF dyes, several vibration bonds of CaO-C₃N₄, such as aromatic C–N stretching and triazine ring modes, have shifted position. This study demonstrated that delocalized electron systems of C₃N₃ and functional groups of CaO-g-C₃N₄ were responsible for the adsorption of BF molecules. In addition, the O–H and NH stretching vibration modes were shifted, demonstrating the interaction of BF molecules with CaO-g-C₃N₄ nanosorbent via hydrogen bonds. Lie et al. demonstrate that sorbents containing pyrazine and imine groups are beneficial to the formation of π - π stacking and hydrogen bonds interactions with organics dyes [65]. Also, the examination of the pH's effect indicates that the electrostatic attraction could not dominate (control) the adsorption mechanism of BF onto the CaO-g-C₃N₄ nanosorbent. The suggested BF adsorption mechanism (Figure 10b) onto the CaO-g-C₃N₄ involves hydrogen bonds and the π - π stacking bridging [66].

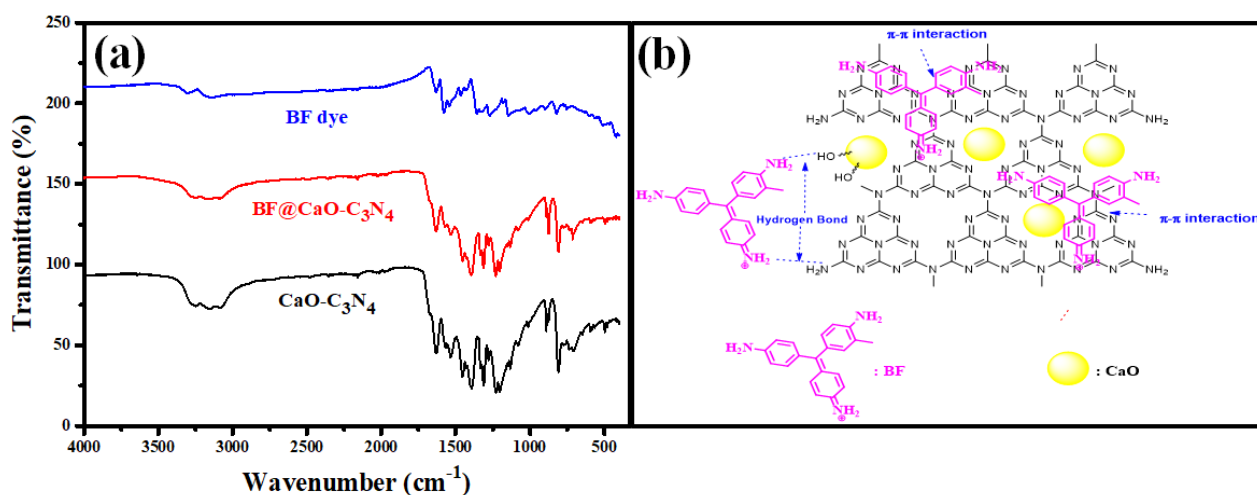


Figure 10. (a) FTIR spectra of BF, CaO-g-C₃N₄ and CaO-g-C₃N₄ @BF and (b) Possible adsorption mechanism of BF dyes onto CaO-g-C₃N₄.

4. Conclusions

Mesoporous CaO-g-C₃N₄ nanosorbent was created using the ultrasonication technique, and it was subsequently employed as an adsorbent to remove BF dyes from wastewater. CaO-g-C₃N₄ nanosorbent removal efficiency was studied by adjusting pH, contact time, and BF concentration. The greatest adsorption capacity observed was 813 $\text{mg}\cdot\text{g}^{-1}$, indicating that the reported data demonstrated outstanding elimination effectiveness toward BF dye. The BF elimination by CaO-g-C₃N₄ nanosorbent was evaluated employed different adsorption and kinetic models, and the best-fitting was committed by the Freundlich adsorption isotherm and PFO kinetics models. The suggested BF adsorption mechanism onto the CaO-g-C₃N₄ involves hydrogen bonds and the π - π stacking bridging. CaO-g-C₃N₄ nanostructures may be easily recovered from solution and were effectively employed for BF elimination in at least four continuous cycles.

Author Contributions: R.B.S.: Conceptualization, Methodology, Formal analysis, Investigation, Visualization. S.R.: Methodology, Formal analysis, Investigation. M.A.B.A.: Methodology, Formal analysis, Investigation. A.A.: Conceptualization, Methodology, Formal analysis, Investigation. A.M.: Conceptualization, Methodology, Formal analysis, Investigation, Visualization. All authors have read and agreed to the published version of the manuscript.

Funding: The authors extend their appreciation to the Deputyship for Research & Innovation, Ministry of Education, Saudi Arabia for funding this research work through the project number (QU-IF-05-01-28461).

Acknowledgments: The authors extend their appreciation to the Deputyship for Research & Innovation, Ministry of Education, Saudi Arabia for funding this research work through the project number (QU-IF-05-01-28461). The authors give thanks to Qassim University for technical support.

Conflicts of Interest: The authors declare no conflict of interest.

References

1. Zamora-Ledezma, C.; Negrete-Bolagay, D.; Figueroa, F.; Zamora-Ledezma, E.; Ni, M.; Alexis, F.; Guerrero, V.H. Heavy metal water pollution: A fresh look about hazards, novel and conventional remediation methods. *Environ. Technol. Innov.* **2021**, *22*, 101504. [[CrossRef](#)]
2. Brown, D. Effects of colorants in the aquatic environment. *Ecotoxicol. Environ. Saf.* **1987**, *13*, 139–147. [[CrossRef](#)] [[PubMed](#)]
3. Hasan, Z.; Jhung, S.H. Removal of hazardous organics from water using metal-organic frameworks (MOFs): Plausible mechanisms for selective adsorptions. *J. Hazard. Mater.* **2015**, *283*, 329–339. [[CrossRef](#)]
4. Zeitoun, M.M.; Mehana, E. Impact of water pollution with heavy metals on fish health: Overview and updates. *Glob. Vet.* **2014**, *12*, 219–231.
5. La Farre, M.; Pérez, S.; Kantiani, L.; Barceló, D. Fate and toxicity of emerging pollutants, their metabolites and transformation products in the aquatic environment. *TrAC Trends Anal. Chem.* **2008**, *27*, 991–1007. [[CrossRef](#)]
6. Thakur, R.H.; Fung, D. Effect of Dyes on the Growth of Food MOLDS 1. *J. Rapid Methods Autom. Microbiol.* **1995**, *4*, 1–35. [[CrossRef](#)]
7. Mirzaei, F.; Nilash, M.M.; Fakhari, A.R. Development of a new electromembrane extraction combined with ion mobility spectrometry for the quantification of malachite green in water samples. *Int. J. Ion Mobil. Spectrom.* **2020**, *23*, 153–160. [[CrossRef](#)]
8. Rajumon, R.; Anand, J.C.; Ealias, A.M.; Desai, D.S.; George, G.; Saravanakumar, M. Adsorption of textile dyes with ultrasonic assistance using green reduced graphene oxide: An in-depth investigation on sonochemical factors. *J. Environ. Chem. Eng.* **2019**, *7*, 103479. [[CrossRef](#)]
9. Ritter, C. Studies of the toxicity of basic fuchsin for certain bacteria. *Am. J. Public Health Nations Health* **1940**, *30*, 59–65. [[CrossRef](#)]
10. Fernandes, E.P.; Silva, T.S.; Carvalho, C.M.; Selvasembian, R.; Chaukura, N.; Oliveira, L.M.; Meneghetti, S.M.P.; Meili, L. Efficient adsorption of dyes by γ -alumina synthesized from aluminum wastes: Kinetics, isotherms, thermodynamics and toxicity assessment. *J. Environ. Chem. Eng.* **2021**, *9*, 106198. [[CrossRef](#)]
11. Casas, N.; Parella, T.; Vicent, T.; Caminal, G.; Sarrà, M. Metabolites from the biodegradation of triphenylmethane dyes by *Trametes versicolor* or laccase. *Chemosphere* **2009**, *75*, 1344–1349. [[CrossRef](#)] [[PubMed](#)]
12. Moumen, A.; Belhocine, Y.; Sbei, N.; Rahali, S.; Ali, F.A.M.; Mehati, F.; Hamdaoui, F.; Seydou, M. Removal of Malachite Green Dye from Aqueous Solution by Catalytic Wet Oxidation Technique Using Ni/Kaolin as Catalyst. *Molecules* **2022**, *27*, 7528. [[CrossRef](#)] [[PubMed](#)]
13. Adam, F.A.; Ghoniem, M.; Diawara, M.; Rahali, S.; Abdulkhair, B.Y.; Elamin, M.; Aissa, M.A.B.; Seydou, M. Enhanced adsorptive removal of indigo carmine dye by bismuth oxide doped MgO based adsorbents from aqueous solution: Equilibrium, kinetic and computational studies. *RSC Adv.* **2022**, *12*, 24786–24803. [[CrossRef](#)]
14. Attia, G.; Rahali, S.; Teka, S.; Fourati, N.; Zerrouki, C.; Seydou, M.; Chehimi, S.; Hayouni, S.; Mbakidi, J.-P.; Bouquillon, S. Anthracene based surface acoustic wave sensors for picomolar detection of lead ions. Correlation between experimental results and DFT calculations. *Sens. Actuators B Chem.* **2018**, *276*, 349–355. [[CrossRef](#)]
15. Pandey, S.; Son, N.; Kim, S.; Balakrishnan, D.; Kang, M. Locust Bean gum-based hydrogels embedded magnetic iron oxide nanoparticles nanocomposite: Advanced materials for environmental and energy applications. *Environ. Res.* **2022**, *214*, 114000. [[CrossRef](#)]
16. Doondani, P.; Jugade, R.; Gomase, V.; Shekhawat, A.; Bambal, A.; Pandey, S. Chitosan/Graphite/Polyvinyl Alcohol Magnetic Hydrogel Microspheres for Decontamination of Reactive Orange 16 Dye. *Water* **2022**, *14*, 3411. [[CrossRef](#)]
17. Gomase, V.; Jugade, R.; Doondani, P.; Deshmukh, S.; Saravanan, D.; Pandey, S. Dual modifications of chitosan with PLK for amputation of cyanide ions: Equilibrium studies and optimization using RSM. *Int. J. Biol. Macromol.* **2022**, *223*, 636–651. [[CrossRef](#)]
18. Rahali, S.; Ben Aissa, M.A.; Khezami, L.; Elamin, N.; Seydou, M.; Modwi, A. Adsorption behavior of Congo red onto barium-doped ZnO nanoparticles: Correlation between experimental results and DFT calculations. *Langmuir* **2021**, *37*, 7285–7294. [[CrossRef](#)]

19. Wu, Y.; Zuo, F.; Zheng, Z.; Ding, X.; Peng, Y. A novel approach to molecular recognition surface of magnetic nanoparticles based on host–guest effect. *Nanoscale Res. Lett.* **2009**, *4*, 738–747. [[CrossRef](#)]
20. Khezami, L.; Aissa, M.A.B.; Modwi, A.; Guesmi, A.; Algethami, F.K.; Bououdina, M. Efficient removal of organic dyes by Cr-doped ZnO nanoparticles. *Biomass Convers. Biorefin.* **2022**, 1–14. [[CrossRef](#)]
21. Khezami, L.; Aissa, M.A.B.; Modwi, A.; Ismail, M.; Guesmi, A.; Algethami, F.K.; Ticha, M.B.; Assadi, A.A.; Nguyen-Tri, P. Harmonizing the photocatalytic activity of g-C₃N₄ nanosheets by ZrO₂ stuffing: From fabrication to experimental study for the wastewater treatment. *Biochem. Eng. J.* **2022**, *182*, 108411. [[CrossRef](#)]
22. Aldaghri, O.; Modwi, A.; Idriss, H.; Ali, M.; Ibnaouf, K. Cleanup of Cd II from water media using Y₂O₃@ g-C₃N₄ (YGCN) nanocomposite. *Diam. Relat. Mater.* **2022**, *129*, 109315. [[CrossRef](#)]
23. Modwi, A.; Elamin, M.R.; Idriss, H.; Elamin, N.Y.; Adam, F.A.; Albadri, A.E.; Abdulkhair, B.Y. Excellent Adsorption of Dyes via MgTiO₃@ g-C₃N₄ Nanohybrid: Construction, Description and Adsorption Mechanism. *Inorganics* **2022**, *10*, 210. [[CrossRef](#)]
24. Modwi, A.; Basith, N.; Ghoniem, M.; Ismail, M.; Aissa, M.B.; Khezami, L.; Bououdina, M. Efficient Pb (II) adsorption in aqueous solution by hierarchical 3D/2D TiO₂/CNNS nanocomposite. *Mater. Sci. Eng. B* **2023**, *289*, 116191. [[CrossRef](#)]
25. Toghan, A.; Abd El-Lateef, H.M.; Taha, K.K.; Modwi, A. Mesoporous TiO₂@ g-C₃N₄ composite: Construction, characterization, and boosting indigo carmine dye destruction. *Diam. Relat. Mater.* **2021**, *118*, 108491. [[CrossRef](#)]
26. Qamar, M.A.; Shahid, S.; Javed, M.; Iqbal, S.; Sher, M.; Akbar, M.B. Highly efficient g-C₃N₄/Cr-ZnO nanocomposites with superior photocatalytic and antibacterial activity. *J. Photochem. Photobiol. A Chem.* **2020**, *401*, 112776. [[CrossRef](#)]
27. Gogoi, D.; Makkar, P.; Ghosh, N.N. Solar light-irradiated photocatalytic degradation of model dyes and industrial dyes by a magnetic CoFe₂O₄-g-C₃N₄ S-scheme heterojunction photocatalyst. *ACS Omega* **2021**, *6*, 4831–4841. [[CrossRef](#)]
28. Varapragasam, S.J.; Andriolo, J.M.; Skinner, J.L.; Grumstrup, E.M. Photocatalytic Reduction of Aqueous Nitrate with Hybrid Ag/g-C₃N₄ under Ultraviolet and Visible Light. *ACS Omega* **2021**, *6*, 34850–34856. [[CrossRef](#)]
29. Cai, W.; Tang, J.; Shi, Y.; Wang, H.; Jiang, X. Improved in situ synthesis of heterostructured 2D/2D BiOCl/g-C₃N₄ with enhanced dye photodegradation under visible-light illumination. *ACS Omega* **2019**, *4*, 22187–22196. [[CrossRef](#)]
30. Alhaddad, M.; Mohamed, R.M.; Mahmoud, M.H. Promoting Visible Light Generation of Hydrogen Using a Sol–Gel-Prepared MnCo₂O₄@ g-C₃N₄ p–n Heterojunction Photocatalyst. *ACS Omega* **2021**, *6*, 8717–8725. [[CrossRef](#)]
31. Paul, D.R.; Gautam, S.; Panchal, P.; Nehra, S.P.; Choudhary, P.; Sharma, A. ZnO-modified g-C₃N₄: A potential photocatalyst for environmental application. *ACS Omega* **2020**, *5*, 3828–3838. [[CrossRef](#)] [[PubMed](#)]
32. Li, Y.; Wang, J.; Yang, Y.; Zhang, Y.; He, D.; An, Q.; Cao, G. Seed-induced growing various TiO₂ nanostructures on g-C₃N₄ nanosheets with much enhanced photocatalytic activity under visible light. *J. Hazard. Mater.* **2015**, *292*, 79–89. [[CrossRef](#)] [[PubMed](#)]
33. Ngullie, R.C.; Alaswad, S.O.; Bhuvanewari, K.; Shanmugam, P.; Pazhanivel, T.; Arunachalam, P. Synthesis and Characterization of Efficient ZnO/g-C₃N₄ Nanocomposites Photocatalyst for Photocatalytic Degradation of Methylene Blue. *Coatings* **2020**, *10*, 500. [[CrossRef](#)]
34. Madhu, B.; Bhagyalakshmi, H.; Shruthi, B.; Veerabhadraswamy, M. Structural, AC conductivity, dielectric and catalytic behavior of calcium oxide nanoparticles derived from waste eggshells. *SN Appl. Sci.* **2021**, *3*, 637. [[CrossRef](#)]
35. Mirghiasi, Z.; Bakhtiari, F.; Darezereshki, E.; Esmaeilzadeh, E. Preparation and characterization of CaO nanoparticles from Ca(OH)₂ by direct thermal decomposition method. *J. Ind. Eng. Chem.* **2014**, *20*, 113–117. [[CrossRef](#)]
36. Tonelli, M.; Gelli, R.; Giorgi, R.; Pierigè, M.I.; Ridi, F.; Baglioni, P. Cementitious materials containing nano-carriers and silica for the restoration of damaged concrete-based monuments. *J. Cult. Herit.* **2021**, *49*, 59–69. [[CrossRef](#)]
37. Yue, Y.; Zhang, P.; Wang, W.; Cai, Y.; Tan, F.; Wang, X.; Qiao, X.; Wong, P.K. Enhanced dark adsorption and visible-light-driven photocatalytic properties of narrower-band-gap Cu₂S decorated Cu₂O nanocomposites for efficient removal of organic pollutants. *J. Hazard. Mater.* **2020**, *384*, 121302. [[CrossRef](#)]
38. Modwi, A.; Abbo, M.; Hassan, E.; Houas, A. Effect of annealing on physicochemical and photocatalytic activity of Cu 5% loading on ZnO synthesized by sol–gel method. *J. Mater. Sci. Mater. Electron.* **2016**, *27*, 12974–12984. [[CrossRef](#)]
39. Li, Y.; Lv, K.; Ho, W.; Dong, F.; Wu, X.; Xia, Y. Hybridization of rutile TiO₂ (rTiO₂) with g-C₃N₄ quantum dots (CN QDs): An efficient visible-light-driven Z-scheme hybridized photocatalyst. *Appl. Catal. B Environ.* **2017**, *202*, 611–619. [[CrossRef](#)]
40. Liu, J.; Liu, M.; Chen, S.; Wang, B.; Chen, J.; Yang, D.-P.; Zhang, S.; Du, W. Conversion of Au (III)-polluted waste eggshell into functional CaO/Au nanocatalyst for biodiesel production. *Green Energy Environ.* **2020**, *7*, 352–359. [[CrossRef](#)]
41. Karuppusamy, I.; Samuel, M.S.; Selvarajan, E.; Shanmugam, S.; Kumar, P.S.M.; Brindhadevi, K.; Pugazhendhi, A. Ultrasound-assisted synthesis of mixed calcium magnesium oxide (CaMgO₂) nanoflakes for photocatalytic degradation of methylene blue. *J. Colloid Interface Sci.* **2021**, *584*, 770–778. [[CrossRef](#)] [[PubMed](#)]
42. Rojas, J.; Toro-Gonzalez, M.; Molina-Higgins, M.; Castano, C. Facile radiolytic synthesis of ruthenium nanoparticles on graphene oxide and carbon nanotubes. *Mater. Sci. Eng. B* **2016**, *205*, 28–35. [[CrossRef](#)]
43. Thomas, A.; Fischer, A.; Goettmann, F.; Antonietti, M.; Müller, J.-O.; Schlögl, R.; Carlsson, J.M. Graphitic carbon nitride materials: Variation of structure and morphology and their use as metal-free catalysts. *J. Mater. Chem.* **2008**, *18*, 4893–4908. [[CrossRef](#)]
44. Mustafa, B.; Modwi, A.; Ismail, M.; Makawi, S.; Hussein, T.; Abaker, Z.; Khezami, L. Adsorption performance and Kinetics study of Pb (II) by RuO₂-ZnO nanocomposite: Construction and Recyclability. *Int. J. Environ. Sci. Technol.* **2022**, *19*, 327–340. [[CrossRef](#)]
45. Li, N.; Dang, H.; Chang, Z.; Zhao, X.; Zhang, M.; Li, W.; Zhou, H.; Sun, C. Synthesis of uniformly distributed magnesium oxide micro-/nanostructured materials with deep eutectic solvent for dye adsorption. *J. Alloys Compd.* **2019**, *808*, 151571. [[CrossRef](#)]

46. Al-Ghouti, M.A.; Razavi, M.M. Water reuse: Brackish water desalination using *Prosopis juliflora*. *Environ. Technol. Innov.* **2020**, *17*, 100614. [[CrossRef](#)]
47. Ayawei, N.; Ebelegi, A.N.; Wankasi, D. Modelling and interpretation of adsorption isotherms. *J. Chem.* **2017**, *2017*, 3039817. [[CrossRef](#)]
48. Oladipo, B.; Govender-Opitz, E.; Ojumu, T.V. Kinetics, Thermodynamics, and Mechanism of Cu (II) Ion Sorption by Biogenic Iron Precipitate: Using the Lens of Wastewater Treatment to Diagnose a Typical Biohydrometallurgical Problem. *ACS Omega* **2021**, *6*, 27984–27993. [[CrossRef](#)]
49. Lagergren, S.K. About the theory of so-called adsorption of soluble substances. *Sven. Vetenskapsakad. Handlingar* **1898**, *24*, 1–39.
50. Chien, S.; Clayton, W. Application of Elovich equation to the kinetics of phosphate release and sorption in soils. *Soil Sci. Soc. Am. J.* **1980**, *44*, 265–268. [[CrossRef](#)]
51. Khezami, L.; Elamin, N.; Modwi, A.; Taha, K.K.; Amer, M.; Bououdina, M. Mesoporous Sn@TiO₂ nanostructures as excellent adsorbent for Ba ions in aqueous solution. *Ceram. Int.* **2022**, *48*, 5805–5813. [[CrossRef](#)]
52. Hameed, B.; Salman, J.; Ahmad, A. Adsorption isotherm and kinetic modeling of 2, 4-D pesticide on activated carbon derived from date stones. *J. Hazard. Mater.* **2009**, *163*, 121–126. [[CrossRef](#)] [[PubMed](#)]
53. El-Sikaily, A.; El Nemr, A.; Khaled, A.; Abdelwehab, O. Removal of toxic chromium from wastewater using green alga *Ulva lactuca* and its activated carbon. *J. Hazard. Mater.* **2007**, *148*, 216–228. [[CrossRef](#)]
54. Ali, I.; Peng, C.; Ye, T.; Naz, I. Sorption of cationic malachite green dye on phylogenetic magnetic nanoparticles functionalized by 3-mercaptopropanoic acid. *RSC Adv.* **2018**, *8*, 8878–8897. [[CrossRef](#)] [[PubMed](#)]
55. Khan, T.A.; Khan, E.A. Removal of basic dyes from aqueous solution by adsorption onto binary iron-manganese oxide coated kaolinite: Non-linear isotherm and kinetics modeling. *Appl. Clay Sci.* **2015**, *107*, 70–77. [[CrossRef](#)]
56. Aissa, B.; Khezami, L.; Taha, K.; Elamin, N.; Mustafa, B.; Al-Ayed, A.; Modwi, A. Yttrium oxide-doped ZnO for effective adsorption of basic fuchsin dye: Equilibrium, kinetics, and mechanism studies. *Int. J. Environ. Sci. Technol.* **2021**, *19*, 9901–9914. [[CrossRef](#)]
57. Guan, Y.; Wang, S.; Wang, X.; Sun, C.; Wang, Y.; Hu, L. Preparation of mesoporous Al-MCM-41 from natural palygorskite and its adsorption performance for hazardous aniline dye-basic fuchsin. *Microporous Mesoporous Mater.* **2018**, *265*, 266–274. [[CrossRef](#)]
58. Kalita, S.; Pathak, M.; Devi, G.; Sarma, H.; Bhattacharyya, K.; Sarma, A.; Devi, A. Utilization of *Euryale ferox* Salisbury seed shell for removal of basic fuchsin dye from water: Equilibrium and kinetics investigation. *RSC Adv.* **2017**, *7*, 27248–27259. [[CrossRef](#)]
59. Bessashia, W.; Berredjem, Y.; Hattab, Z.; Bououdina, M. Removal of Basic Fuchsin from water by using mussel powdered eggshell membrane as novel bioadsorbent: Equilibrium, kinetics, and thermodynamic studies. *Environ. Res.* **2020**, *186*, 109484. [[CrossRef](#)]
60. Mohammed, B.B.; Hsini, A.; Abdellaoui, Y.; Abou Oualid, H.; Laabd, M.; El Ouardi, M.; Addi, A.A.; Yamni, K.; Tijani, N. Fe-ZSM-5 zeolite for efficient removal of basic Fuchsin dye from aqueous solutions: Synthesis, characterization and adsorption process optimization using BBD-RSM modeling. *J. Environ. Chem. Eng.* **2020**, *8*, 104419. [[CrossRef](#)]
61. Huang, L.; Kong, J.; Wang, W.; Zhang, C.; Niu, S.; Gao, B. Study on Fe (III) and Mn (II) modified activated carbons derived from *Zizania latifolia* to removal basic fuchsin. *Desalination* **2012**, *286*, 268–276. [[CrossRef](#)]
62. Ghoniem, M.G.; Ali, F.A.M.; Abdulkhair, B.Y.; Elamin, M.R.A.; Alqahtani, A.M.; Rahali, S.; Ben Aissa, M.A. Highly selective removal of cationic dyes from wastewater by MgO nanorods. *Nanomaterials* **2022**, *12*, 1023. [[CrossRef](#)] [[PubMed](#)]
63. AbuMousa, R.A.; Khezami, L.; Ismail, M.; Ben Aissa, M.A.; Modwi, A.; Bououdina, M. Efficient Mesoporous MgO/g-C₃N₄ for Heavy Metal Uptake: Modeling Process and Adsorption Mechanism. *Nanomaterials* **2022**, *12*, 3945. [[CrossRef](#)] [[PubMed](#)]
64. Margaretha, Y.Y.; Prastyo, H.S.; Ayucitra, A.; Ismadji, S. Calcium oxide from *Pomacea* sp. shell as a catalyst for biodiesel production. *Int. J. Energy Environ. Eng.* **2012**, *3*, 33. [[CrossRef](#)]
65. Li, J.; Wang, B.; Chang, B.; Liu, J.; Zhu, X.; Ma, P.; Sun, L.; Li, M. One new hexatungstate-based binuclear nickel (II) complex with high selectivity adsorption for organic dyes. *J. Mol. Struct.* **2021**, *1231*, 129674. [[CrossRef](#)]
66. Feng, Y.; Chen, G.; Zhang, Y.; Li, D.; Ling, C.; Wang, Q.; Liu, G. Superhigh co-adsorption of tetracycline and copper by the ultrathin g-C₃N₄ modified graphene oxide hydrogels. *J. Hazard. Mater.* **2022**, *424*, 127362. [[CrossRef](#)]

Disclaimer/Publisher's Note: The statements, opinions and data contained in all publications are solely those of the individual author(s) and contributor(s) and not of MDPI and/or the editor(s). MDPI and/or the editor(s) disclaim responsibility for any injury to people or property resulting from any ideas, methods, instructions or products referred to in the content.